Trapped-hydrogen-induced energy loss in tin-based hybrid perovskite solar cells

Yuhang Liang,[1,2] *Xiangyuan Cui*,[3,*] *Feng Li*,[2] *Catherine Stampfl*,[2] *Simon P. Ringer*,[3] *Jun Huang*,[1,*] *Rongkun Zheng*[2,*]

[1] School of Chemical and Biomolecular Engineering, The University of Sydney, NSW 2006, Australia

[2] School of Physics, The University of Sydney, NSW 2006, Australia

[3]School of Aerospace, Mechanical and Mechatronic Engineering, The University of Sydney, NSW 2006, Australia

*Xiangyuan Cui: carl.cui@sydney.edu.au

*Jun Huang: jun.huang@sydney.edu.au

*Rongkun Zheng: rongkun.zheng@sydney.edu.au

Abstract

The hitherto subdued power conversion efficiencies of Sn-based hybrid perovskite solar cells are generally attributed to severe nonradiative recombination; however, the responsible deep-level defects are still unclear. Here, we report an important nonradiative energy loss mechanism in the prototypical $FASnI_3$ (FA= $HC(NH_2)_2$, formamidinium). High-density Tin vacancies (V_{Sn}) can effectively capture hydrogen to form $V_{Sn}-H_2$ complexes that act as highly detrimental nonradiative recombination centers. We quantitatively show that they can give rise to strong carrier recombination and thus energy loss due to a high nonradiative recombination rate constant. These key findings identify a hidden yet critical origin for the low performance of $FASnI_3$-based devices and highlight the significance of controlling the hydrogen environment in the development of broad high-efficiency non-toxic halide perovskite device applications.

Keywords: Sn-based perovskite solar cells, optoelectronics, nonradiative recombination center, hydrogen defects, density functional theory

Introduction

Owing to the unique photophysical properties, low-cost organic-inorganic hybrid perovskites have drawn intensive attention in the optoelectronic community [1–4]. In particular, rapid progress has been demonstrated in perovskite solar cells with a power conversion efficiency (PCE) exceeding 25.8% [4], which is already close to that of single-crystal silicon cells (26.6%) [5]. Nevertheless, the toxicity of lead (Pb) to the human body and environment poses a significant challenge for the further commercialization of the perovskite photovoltaic technology [6,7]. Isovalent tin (Sn) has been regarded as one of the most appropriate replacements for Pb in the perovskite layers among various nontoxic alternatives. Sn-based hybrid perovskites, such as methylammonium tin iodide ($MASnI_3$) and formamidinium tin iodide ($FASnI_3$), have the narrower optical bandgaps of 1.20-1.40 eV [8], closer to the Shockley-Queisser (S-Q) limit (1.34 eV) [9] than those of the Pb-based counterparts (1.5-1.7 eV), indicating the potential for higher efficiency limits. In addition, Sn-based perovskite materials exhibit high absorption coefficients [10] and small exciton binding energies [11]. Taking advantage of these merits, Sn-based perovskites hold great promise for lead-free perovskite photovoltaics and other device applications.

However, since the early demonstration of $MASnI_3$ perovskite solar cells yielding PCE of around 6% in 2014 [12] and 9% in 2018 [11], respectively, the highest PCE only reached 14% in $FASnI_3$-based solar cells [13], outperforming other Pb-free candidates but still lagging significantly behind the Pb-based counterparts. Defect-induced nonradiative charge recombination is generally considered an important loss mechanism for Sn-based perovskite solar cells [8,12,14–16]. As compared to the Pb-based halide perovskites, the much faster crystallization process and easier oxidation of the Sn-based halide perovskites lead to the formation of a high density of defects, specifically deep-level nonradiative recombination centers [8,12,14–16]. Notably, Ng *et al.* [17,18] reported that the pristine $FASnI_3$ active layer displays a huge deep-level state density up to $\sim 10^{20}$ cm^{-3}, which is around five orders of magnitude higher than that in the Pb-based counterparts [19]. The measured nonradiative recombination rate often reaches up to $\sim 10^{9}\ \mathrm{s}^{-1}$ [20–22], compared to $10^{6} - 10^{7}\ \mathrm{s}^{-1}$ typically measured in the Pb-based perovskites [21]. The severe nonradiative recombination losses in Sn-based halide perovskites significantly hinder the photo-generated carrier transport and reduce the open-circuit voltage (V_{OC}), resulting in inferior solar cell efficiencies.

Accurately identifying the potential deep-level defects that act as detrimental nonradiative recombination centers is crucial for further optimizations of Sn-based perovskite (e.g., $FASnI_3$) devices. Experimental reports [17] have indicated that adding excess Sn halides, such as SnI_2 or SnF_2, namely a Sn-rich growth condition, can reduce the density of deep-trap states and the recombination rate to a certain extent, and thus improve the V_{OC} and PCE of $FASnI_3$-based solar cells, though such a strategy cannot completely remedy the problem. Due to this dependence, it has been proposed that the observed nonradiative recombination is closely associated with the emergence of high-density intrinsic Sn vacancies (V_{Sn}) [23,24] as a result of the facile oxidation of Sn^{2+} into Sn^{4+} [25]. However, a first-principles investigation reveals that V_{Sn} acts as a shallow defect in $FASnI_3$ [26]. Thus far the microscopic origin of the detrimental deep-level defects in $FASnI_3$ remains mysterious.

In addition to the intrinsic defects, hydrogen defects can be a candidate. As found in many traditional semiconductors [27,28], experimental [29–31] and theoretical [32–37] studies have reported the existence of interstitial hydrogen species in the lattice of the hybrid lead halide perovskites, especially under the moisture conditions. In particular, Seok *et al.* [38] proposed that the long-term instability of the perovskite-based devices can be partially attributed to the accumulation of hydrogen owing to its electrical activity and high mobility. Here, based on first-principles hybrid functional calculations, we found that, in $FASnI_3$, hydrogen prefers to exist in a “hidden” form: hydrogen interstitials tend to be trapped within the abundant native Sn vacancies and thus form $V_{Sn} - H_2$ complexes. Significantly, while neither V_{Sn} nor H_2 are deep-level defects in $FASnI_3$, the strong chemical interaction within the $V_{Sn} - H_2$ complex results in a deep transition level within the bandgap with a large capture coefficient of 2.1×10^{-9} cm^3 s^{-1}, which can cause sizable energy loss.

Results and discussion

Figure 1a shows the stability phase diagram of $FASnI_3$ and derivatives relative to the chemical potentials ($\Delta\mu_I$ and $\Delta\mu_{Sn}$). The thermodynamically stable $FASnI_3$ is represented as the red region with respect to its elemental phases (I, Sn, and FA) and the competing secondary phases (SnI_2, SnI_4, FAI, and FA_2SnI_6). Within the red region, three representative sets of chemical potentials, as marked as points A, B, and C, correspond to the Sn-rich/I-poor, moderate, and Sn-poor/I-rich growth conditions, respectively. Since there have been few reports on $FASnI_3$ grown under the Sn-poor growth conditions, we will focus on the moderate and Sn-rich growth conditions, which stand for the pristine $FASnI_3$ film and that with excess Sn treatment in experiment, respectively. **Figure 1b** shows the formation energies of six dominant native defects [26] under the moderate and Sn-rich growth conditions by using the HSE+SOC+TS scheme, and those under the Sn-poor conditions are shown in **Figure S1** for comparison. They are three types of vacancies (V_{Sn}, V_I, V_{FA}), two interstitials (FA_i, I_i), and one antisite defect (I_{Sn}, namely Sn substituted by I), respectively. Our results are qualitatively similar to prior semi-local generalized gradient approximation studies [26] except that the transition energy level of I_{Sn} is located at 0.06 eV above the valence band maximum (VBM) in the current study. Consistent with the experimental reports [11], V_{Sn} emerges as the major defect in $FASnI_3$ with extremely low formation energy and serves as a robust shallow acceptor. Particularly, under the moderate conditions, the formation energy of V_{Sn} is much lower than that of the lowest-energy donor V_I, with the Fermi level (E_F) being pinned at VBM+ 0.18 eV, accounting for the high background-hole concentration (i.e. the self-*p*-doping effect) observed for the pristine film [8,20]. Under the Sn-rich conditions, $FASnI_3$ will be an intrinsic (low-conductivity) semiconductor as V_I can compensate for V_{Sn}, and the E_F is thus pinned at the middle of the bandgap (VBM+0.78 eV). In contrast to the deep-level property in $MAPbI_3$ [39], I_i behaves as a shallow defect in $FASnI_3$, as reported in $MASnI_3$ [40] due to the higher band edge energies of hybrid Sn perovskite compared with the Pb-based counterparts [40,41]. Other low-energy intrinsic defects do not create a transition energy level in the bandgap either. These dominant native defects thus are not responsible for the observed nonradiative recombination of the $FASnI_3$-based devices.

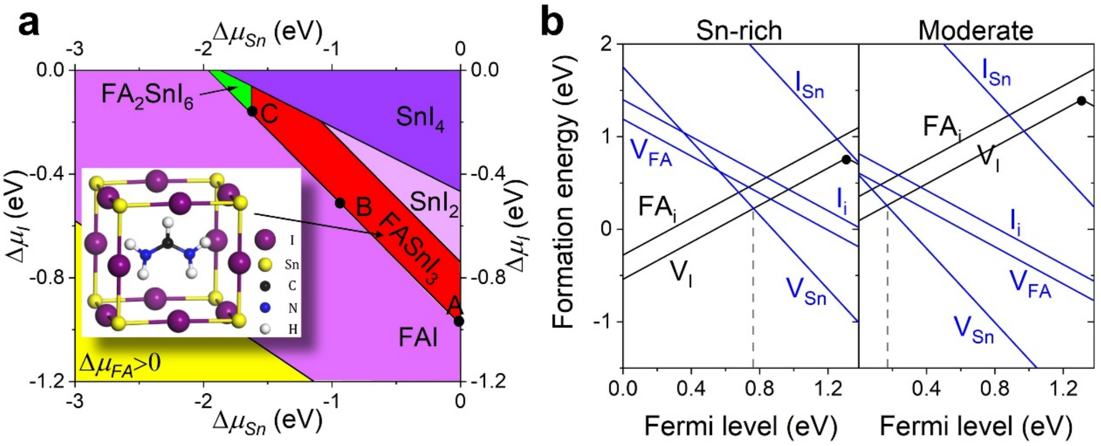

Figure 1. (**a**) Calculated stability phase diagram of FASnI3 as a function of the chemical potentials of Sn (μ_{Sn}) and iodine (μ_I). The red region is the thermodynamically stable range for the equilibrium growth of FASnI3. Points A, B, and C are three representative sets of chemical potentials. The inset shows the crystal structure of the FASnI3 perovskite. (**b**) Formation energies of six dominant native defects ($\mathrm{V_{Sn}}$, $\mathrm{V_I}$, $\mathrm{V_{FA}}$, $\mathrm{FA_i}$, $\mathrm{I_{Sn}}$, and $\mathrm{I_i}$) in FASnI3 as a function of the Fermi level under the Sn-rich and moderate conditions, corresponding to the chemical potentials of points A and B in (**a**), respectively. Black and blue lines represent the donor and acceptor defects, respectively. The vertical dashed lines represent the location at which the Fermi level is pinned, based on the condition of charge neutrality between the lowest-energy defects.

We then investigated an important, but hitherto overlooked type of defect, hydrogen. To analyze its stability in FASnI3, we systematically studied various hydrogen-related defects and complexes, including isolated atomic and molecular H, and their interaction with different native defects. For hydrogen incorporated into the vacancies, they can form either substitutions or vacancy-hydrogen defect complexes, depending on the optimized atomic configurations (for example, $\mathrm{V_I-H}$ complex of the off-center position in **Figure S2a** and substitutional $\mathrm{(H_2)_I}$ of the in-center position in **Figure S2b**). The formation energies of various low-energy forms are presented in **Figure 2a**, and the other higher-energy complexes are shown in **Figure. S3**. In FASnI3, atomic hydrogen $\mathrm{H_i}$ tends to be ionized into the positively charged state, i.e., proton $\mathrm{H_i^+}$, in the whole range of EF. In contrast, the molecular form of hydrogen interstitial $\mathrm{H_2}$ behaves as an electrically inactive defect, as reported in many traditional semiconductors [28].

Under the Sn-rich growth conditions, where the E_F is pinned at 0.78 eV above the VBM as mentioned above, the formation energy of H_2 are lower than that of H_i^+, and thus H_2 molecule is expected to be formed via the recombination of protons as reported in ZnO [42]. The calculated binding energy is: $H_i^+ + H_i^+ + 2e^- \xrightarrow{-0.96\ \mathrm{eV}} H_2$, where e^- is the electron with the energy of $E_F = 0.78$ eV. For comparison, under the Sn-moderate conditions, the material exhibits a strong *p*-type character with a high hole concentration, and H_i^+ has lower formation energy than H_2. That is, under such a hole-rich condition, H_2 tends to disassociate into H_i^+. The binding energy of the process is $H_2 - 2e^- \xrightarrow{-0.42\ \mathrm{eV}} 2H_i^+$ with the energy of the electron e^- at $E_F = 0.18$ eV.

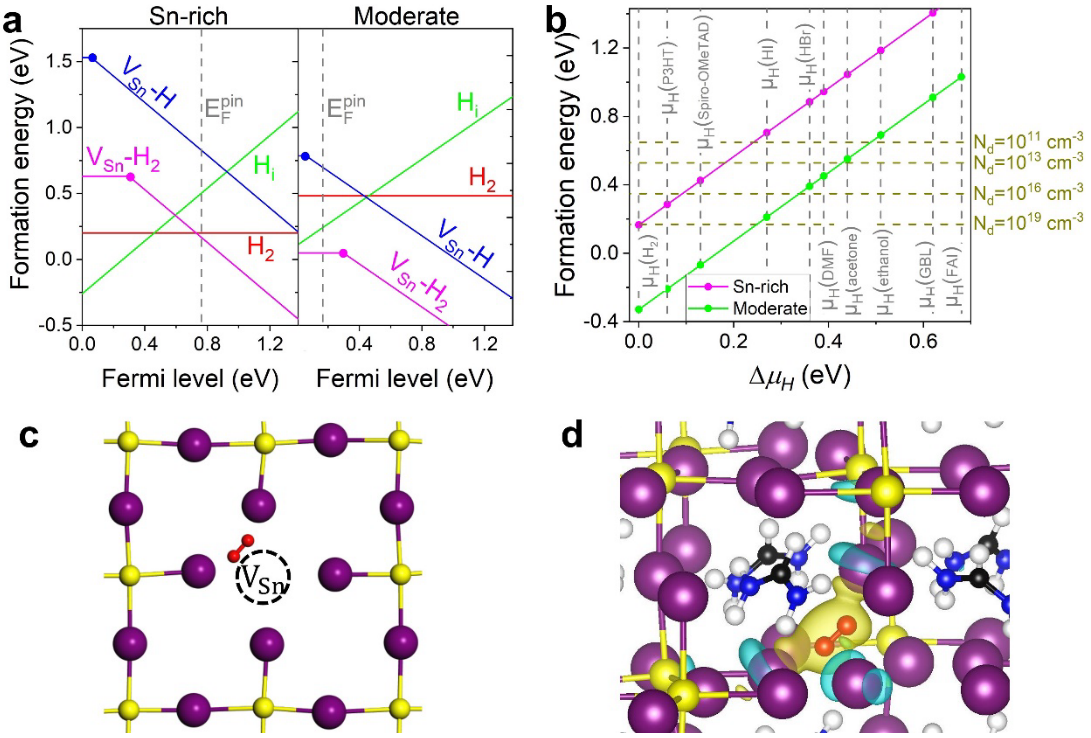

Figure 2. (**a**) Formation energies as a function of the Fermi level for hydrogen in the interstitial atomic hydrogen H_i, interstitial molecular hydrogen $(H_2)_i$, and Sn vacancy-hydrogen complexes $V_{Sn} - H$ and $V_{Sn} - H_2$, under the Sn-rich and Sn-moderate synthesis conditions in $FASnI_3$. The chemical potential of H is set at half of the total energy of an isolated H_2 molecule, namely the H-rich conditions, as a reference. The vertical dashed lines are the pinned Fermi levels by native low-energy defects as shown in **Figure 1b**. (**b**) Calculated formation energy of the deep-level $V_{Sn} - H_2$ complex as

a function of the relative hydrogen chemical potential in various potential H sources, under the two representative Sn conditions. The corresponding defect densities (N_d) at room temperature are denoted. (**c**) Local atomic structures of the $(\mathrm{V_{Sn}}-\mathrm{H_2})^0$ complexes in $FASnI_3$ perovskite lattice. (**d**) Calculated isosurfaces of the charge density differences for a $(\mathrm{V_{Sn}}-\mathrm{H_2})^0$ complex, where electrons are relocated from the yellow to the blue regions. The isosurfaces are taken at 0.01 $|e|/\text{Å}^3$. The notations of atoms are as those in **Figure 1** and the hydrogen interstitials are highlighted in red.

Further, we found another dominant form of hydrogen: these isolated hydrogen interstitials can interact strongly with the abundant native Sn vacancies, resulting in defect complexes made of the hydrogen species trapped into $\mathrm{V_{Sn}}$, namely, $\mathrm{V_{Sn}}-\mathrm{H}$ and $\mathrm{V_{Sn}}-\mathrm{H_2}$, as shown in **Figure 2a**. In the case of hydrogen interacting with other native vacancies, $\mathrm{V_I}$ and $\mathrm{V_{FA}}$, the related substitutions and complexes exhibit considerably higher formation energies (> 1.5 eV) regardless of the growth conditions, as shown in **Figure S2**. They are thus expected to play an insignificant role in $FASnI_3$.

The negatively charged state (-1) of $\mathrm{V_{Sn}}-\mathrm{H}$ complex is a shallow acceptor with a transition level $\varepsilon(0/-1)$ at VBM+0.06 eV. Significantly, regardless of the growth conditions, the $\mathrm{V_{Sn}}-\mathrm{H_2}$ complex is energetically more favorable compared with $\mathrm{V_{Sn}}-\mathrm{H}$ and gives rise to a deep charge-state transition level in the bandgap located at VBM+0.30 eV, which is similar to the experimentally measured energetic depth (~0.25 eV) of the trap states by the thermally stimulated current (TSC) studies [17]. In particular, under the moderate growth conditions, the formation energy of $\mathrm{V_{Sn}}-\mathrm{H_2}$ is ~ 0.76 eV lower than that of $\mathrm{V_{Sn}}-\mathrm{H}$, suggesting that $(\mathrm{V_{Sn}}-\mathrm{H})^-$ tends to capture an additional $\mathrm{H_i^+}$ to form $\mathrm{V_{Sn}}-\mathrm{H_2}$. Indeed, the calculated binding energy of $(\mathrm{V_{Sn}}-\mathrm{H_2})^0$ with respect to $(\mathrm{V_{Sn}}-\mathrm{H})^-$ and $\mathrm{H_i^+}$, is 1.36 eV. $\mathrm{V_{Sn}}-\mathrm{H}$ serves as a metastable species. Under Sn-rich growth conditions, favoring $\mathrm{H_2}$ as the dominant hydrogen interstitial, $\mathrm{V_{Sn}}-\mathrm{H_2}$ is expected to be formed via the direct trapping of $\mathrm{H_2}$ into $\mathrm{V_{Sn}}$ and the related binding energy is $\mathrm{V_{Sn}^{2-}}+\mathrm{H_2}-e^- \xrightarrow{-0.45\ \mathrm{eV}} (\mathrm{V_{Sn}}-\mathrm{H_2})^-$. Furthermore, we investigated the possibility of additional atomic or molecular hydrogen incorporation into a $\mathrm{V_{Sn}}-\mathrm{H_2}$ and confirmed their formation is energetically unfavored in $FASnI_3$ (see **Table S1**). Therefore, in equilibrium, the $\mathrm{V_{Sn}}-\mathrm{H_2}$ complexes are the dominant forms of hydrogen in $FASnI_3$ in addition to the traditionally believed isolated hydrogen interstitials of H_i and H_2.

To reveal the practical H environment during the growth and post-processing of the perovskites, we computed the formation energies of $V_{Sn} - H_2$, as a function of the relative H chemical potentials in various potential hydrogen sources, under the two representative Sn growth conditions, as shown in **Figure 2b**. The defect densities at different formation energies were calculated based on the thermal equilibrium equation. In addition to H_2 gas doping, the dehydrogenation of the organic hole-transporting materials (such as spiro-OMeTAD and P3HT), the widely used solvents (such as DMF, acetone, ethanol), and even the additives of HI and HBr, can serve as the potential source of unintentional H contamination. Note that, under the same H conditions, the density of deep-level $V_{Sn} - H_2$ under the Sn-rich growth conditions is lower than that under the moderate conditions, which is consistent with the general experimental observation of reduced deep-state density and nonradiative recombination rate in the $FASnI_3$ layers after excess Sn treatment [17,20]. Moreover, regardless of the Sn growth conditions, the density of $V_{Sn} - H_2$ can be up to $> 10^{19} cm^{-3}$ even under the H-rich conditions at room temperature.

Notably, neither native V_{Sn} nor H_2 are deep-level defects in $FASnI_3$, while their combined defect complexes exhibit deep-level characteristics. In V_{Sn}, the incorporated molecular H_2 resides between two I atoms with longer molecular bond lengths of 0.98 Å for $(V_{Sn} - H_2)^0$ and 0.91 Å for $(V_{Sn} - H_2)^-$, respectively, as compared to 0.77 Å for the interstitial sites and 0.75 Å for the free H_2, respectively, resulting in a structural distortion of the lattice (**Figure 2c**). This indicates the strong chemical interactions between each H and its nearby I atoms. We further studied the charge density difference during the formation of $V_{Sn} - H_2$ in $FASnI_3$. The charge originally located on the hydrogen species is redistributed to the nearest I atoms of the V_{Sn} (**Figure 2d**), confirming the strong chemical interactions between the trapped H_2 and V_{Sn} - giving rise to a deep transition level in the bandgap.

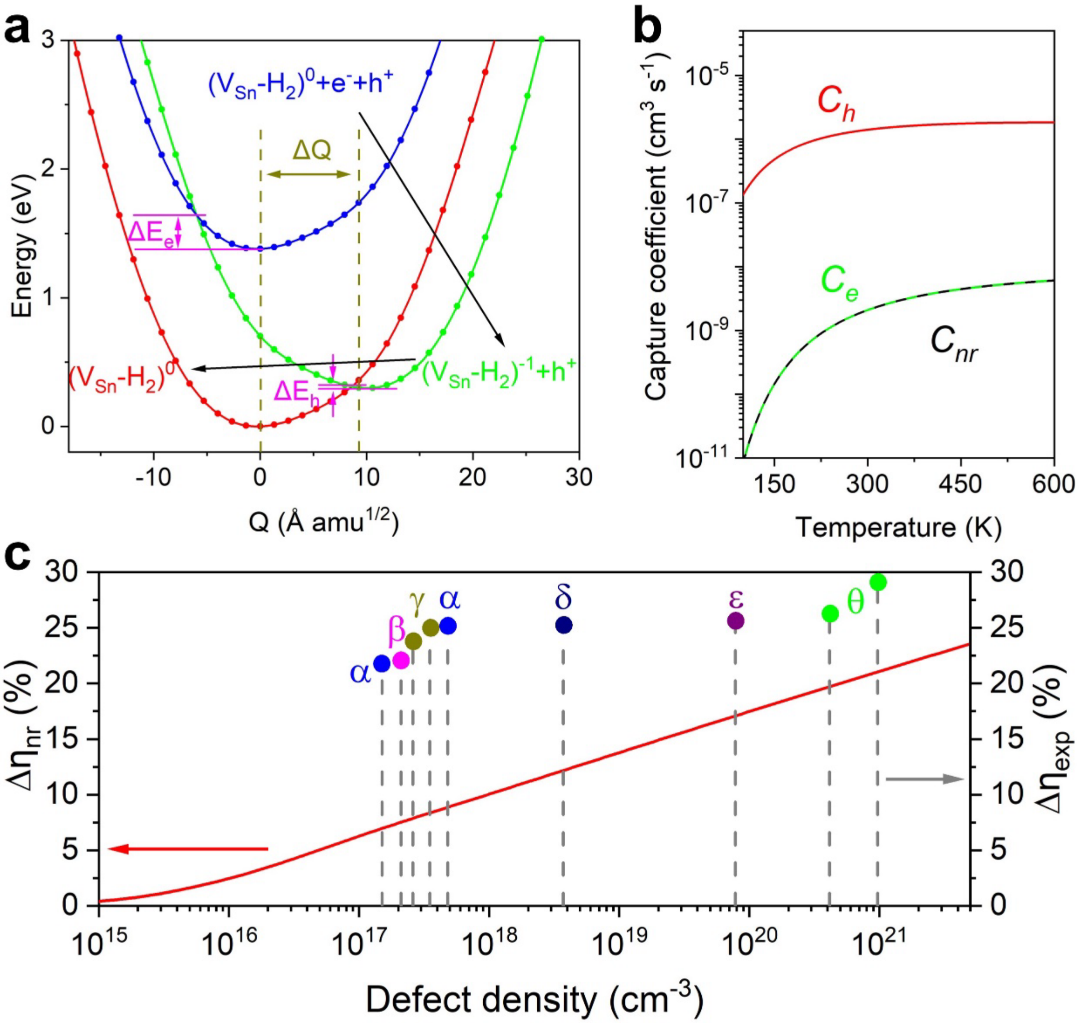

Figure 3. (**a**) Configuration coordinate diagrams for the $(0/-)$ charge-state transition of the $\mathrm{V_{Sn}-H_2}$ complex. The generalized coordinate (Q) of each configuration is defined by its difference from the reference [43]: $Q=\sqrt{\sum_a m_a(R_a-R_{f,a})^2}$, where m_a and R_a are the mass and the Cartesian coordinate of atom a; subscript f stands for the final state of the charge transition. (**b**) Nonradiative capture coefficient of the $\mathrm{V_{Sn}-H_2}$ complex as a function of temperature in $\mathrm{FASnI_3}$. (**c**) The calculated and experimental PCE losses: the left-Y axis stands for the calculated nonradiative-induced PCE loss ($\Delta\eta_{nr}$) by the $\mathrm{V_{Sn}-H_2}$ complexes as a function of the complex density at room temperature. The right-Y axis stands for the experimentally practical solar cell PCE losses relative to the S-Q efficiency limit of $\mathrm{FASnI_3}$ (i.e., $\Delta\eta_{exp}$= 33.09% – the reported PCE values). The measured deep-level trap densities and PCE values of α are taken from Ref. [15], β from Ref. [44], γ from Ref. [45], δ from Ref. [18], ε from Ref. [46], and θ from Ref. [17].

To quantitatively and explicitly assess the effects of deep-level $\mathrm{V_{Sn}-H_2}$ complexes on the nonradiative electron-hole recombination, we further calculated its carrier capture coefficient by following the established multi-phonon emission methodology [43,47]. We first performed the semi-classical analysis and studied the configuration coordinate diagram (CCD) for the charged-state transition, which maps the potential energy surface (PES) of $\mathrm{(V_{Sn}-H_2)^0}$ and $\mathrm{(V_{Sn}-H_2)^-}$ as a function of a generalized coordinate (Q), as shown in **Figure 3a**. The CCD study not only provides a convenient illustration of a complete cycle of nonradiative capture but also derives important input parameters for further nonradiative coefficient calculations [47]. As shown in **Figure 3a**, starting from the neutral-state $\mathrm{(V_{Sn}-H_2)^0}$ with a free electron (e^-) at the CBM and a hole (h^+) at the VBM (depicted by the blue curve), $\mathrm{(V_{Sn}-H_2)^0}$ captures an electron and transits to negative-charged $\mathrm{(V_{Sn}-H_2)^-}$ complex (depicted by the green curve). Subsequently, the negative-charged $\mathrm{(V_{Sn}-H_2)^-}$ captures a hole and relaxes back to neutral $\mathrm{(V_{Sn}-H_2)^0}$ (depicted by the red curve). Semi-classically, these processes are required to overcome kinetic barriers, that is, the energy required to cross the intersection of the PES between the initial and final charge states in the configuration coordinate diagram, which thus determines the capture rates. Our calculations show that electron capture by $\mathrm{(V_{Sn}-H_2)^0}$ is required to overcome an energy barrier (ΔE_e) of ~ 0.26 eV. In comparison, the PES intersection of the hole capture process goes through the minimum of the PES of the initial state (the bottom of the green curve). Correspondingly, the hole capture barrier (ΔE_h) for $\mathrm{(V_{Sn}-H_2)^-}$ is very small $(\sim 0.06$ eV), indicative of a significantly faster hole capture process.

We then calculated the nonradiative capture coefficient according to the strength of the electron–phonon coupling and the vibronic overlap between potential energy surfaces [43]. **Figure 3b** shows the calculated electron capture coefficient $(\mathrm{C_e})$, hole capture coefficient $(\mathrm{C_h})$, and the nonradiative recombination coefficient $(\mathrm{C_{nr}})$ as the function of temperature. As expected, $\mathrm{(V_{Sn}-H_2)^0}$ exhibits slower electron capture due to the relatively small capture coefficient, $C_e = 2.1 \times 10^{-9}\ \mathrm{cm^3\ s^{-1}}$ at room temperature; hole capture by $\mathrm{(V_{Sn}-H_2)^-}$ is much faster with a coefficient $(\mathrm{C_h})$ of $1.4 \times 10^{-6}\ \mathrm{cm^3\ s^{-1}}$ at room temperature. Based on the balance between electron and hole captures under steady-state conditions, the nonradiative coefficient is $\mathrm{C_{nr}} = \frac{\mathrm{C_e C_h}}{\mathrm{C_e+C_h}}$.

At room temperature, the $\mathrm{C_{nr}}$ value of the deep-level $\mathrm{V_{Sn}-H_2}$ complex is $2.1 \times 10^{-9}\ \mathrm{cm^3\ s^{-1}}$, compared with that of $\mathrm{I_i}$ in $\mathrm{MAPbI_3}$ ($7 \times 10^{-9}\ \mathrm{cm^3\ s^{-1}}$) [39], which has been shown to be a dominant nonradiative recombination center to affect the $\mathrm{MAPbI_3}$-based device performance. The nonradiative recombination rate constant A hence can be determined by both the defect density (N) and the capture coefficient per defect ($\mathrm{C_{Tot}}$), yielding: $\mathrm{A = N \times C_{Tot}}$, which stands for the number of nonradiative recombination events unit time, namely, the reciprocal of nonradiative lifetime τ_{nr}.

To further understand the impact of the nonradiative recombination on the device performance, we calculated the resultant PCE loss ($\Delta\eta_{nr}$) based on the detailed balance limit, which is commonly known as the S-Q limit [9]. For an ideal solar cell under steady-state conditions, the photocurrent can be expressed as $J(V) = J_P - J_{rad}(V)$, where $J_P \cong q\int_{E_g}^{\infty}\frac{2\pi}{h^3c^2}\frac{E^2}{e^{(\frac{E}{KT_{sun}})}-1}dE$ is the current density that is generated by the incident light, and $J_{rad}(V) \cong q\int_{E_g}^{\infty}\frac{2\pi}{h^3c^2}\frac{E^2}{e^{(\frac{E-qV}{KT_{cell}})}-1}dE$ is the radiative recombination current density. V stands for the applied voltage and is equal to the splitting of the Fermi levels $qV = E_F^n - E_F^p$. q, h, K, and c are the elementary charge, Planck's constant, Boltzmann constant, and speed of light, respectively. The electrical output power density of the solar cell is given by $P_{out}(V) = J(V) \times V$, and hence, the light to electricity PCE in the case of the radiative limit can be calculated by $\eta = \frac{MAX(P_{out}(V))}{P_{in}} = \frac{MAX(J(V)\times V)}{P_{in}}$, where the input sun power density can be given by $P_{in} \cong \frac{2\pi}{h^3c^2}\int_0^{\infty}\frac{E^3dE}{e^{(\frac{E}{KT_{sun}})}-1}$. For $\mathrm{FASnI_3}$ with a bandgap of $E_g = 1.38$ eV, under the standard air mass 1.5G spectrum, the PCE of the solar cell can reach a maximum value (S-Q efficiency limit) of $\eta \sim 33.09\%$ at room temperature, which agrees with that reported in Ref. [48].

In the presence of the nonradiative recombination from the $\mathrm{V_{Sn}-H_2}$ complexes, the steady-state $J(V)$ characteristic of the solar cell will be described by: $J(V') = J_P - J_{rad}(V') - J_{nr}(V')$, where the new term of $J_{nr}(V') \cong qd\mathrm{A}n_i e^{(\frac{qV'}{2KT_{cell}})}$ describes the current density loss due to the nonradiative recombination. For the thickness (d) and intrinsic carrier density (n_i) of the perovskite active layer, we adopted the representative values of $d \sim 300\,\text{nm}$ and $n_i \sim 10^7 \text{cm}^{-3}$ [20], respectively. Notably, the Auger recombination can have a negligible impact on the perovskite solar cells due to a relatively low carrier density [49], and thus the nonradiative loss is dominated by the defect-induced process with the nonradiative recombination rate constant being the aforementioned $\text{A} = \text{NC}_{\text{Tot}}$. Similarly, with the electrical output power density of the solar cell of $P_{out}(V') = J(V') \times V'$, the nonradiative-induced PCE loss by the $\text{V}_{\text{Sn}} - \text{H}_2$ complexes can be obtained with $\Delta\eta_{nr} = \eta - \eta' = \frac{MAX(P_{out}(V)) - MAX(P_{out}(V'))}{P_{in}}$.

Figure 3c shows the calculated $\Delta\eta_{nr}$ due to the $\text{V}_{\text{Sn}} - \text{H}_2$ complexes as a function of the defect density at room temperature. As expected, a higher $\text{V}_{\text{Sn}} - \text{H}_2$ density causes higher PCE loss $\Delta\eta_{nr}$, for a certain thickness of FASnI_3 (300 nm used in the current calculation). Our calculated nonradiative efficiency loss induced by $\text{V}_{\text{Sn}} - \text{H}_2$ complexes can be up to $\sim 11\%$ at room temperature at the representative defect density of $\sim 10^{18}$ cm^{-3}. Such a density is possible as mentioned above. A higher defect density can even result in a larger PCE loss especially for the pristine FASnI_3 layers mostly under the moderate growth conditions (with negative formation energies of $\text{V}_{\text{Sn}} - \text{H}_2$ occurring under the H-rich conditions as shown in **Figure 2b**). To reduce the PCE loss to a negligible level, we need to suppress the deep-level defects to $\sim 10^{15}$ cm^{-3}, under which the resultant $\Delta\eta_{nr}$ would be less than 1%.

To correlate our calculated results with experiments, we collected representative experimental PCE and trap density values from literature [17,18,44,44,46], and calculated PCE losses by comparing experimental PCE values with the S-Q limit ($\Delta\eta_{exp}$= 33.09% – the reported PCE values), and plotted them as dots in **Figure 3c**. The experimentally observed deep-level defect densities in the FASnI_3 active layers vary from 10^{17} cm^{-3} to 10^{21} cm^{-3}, and significantly, these devices have low PCE with $\Delta\eta_{exp} > 20\%$. The discrepancy between $\Delta\eta_{nr}$ and $\Delta\eta_{exp}$ originates from their different scopes: the former is the PCE loss solely induced by nonradiative recombination via $\text{V}_{\text{Sn}} - \text{H}_2$, while the latter is the PCE loss due to all the sources including the bulk, surface, and grain boundary recombination [50,51], and other types of energy losses (e.g., the device polarization due to ionic accumulation [50], and the energy level mismatch [52]). In particular, surface and grain boundaries are often significant as they provide the avenue for the segregation of some defects, which may behave differently compared to those in the bulk [50,51,53]. Although there could be other detrimental recombination centers in $FASnI_3$, $V_{Sn}-H_2$ with its induced energy loss offers an explanation for the experimental observation of Sn-conditions dependence of the recombination rate. Furthermore, it was noticeable that the trends of the PCE enhancement via defect passivation reported in Ref. [15] (denoted as α in the figure) and Ref. [17] (denoted as θ in the figure) are in agreement with the trend of the $\Delta\eta_{nr}$ reduction predicted in **Figure 3c**. These results indicate that $V_{Sn}-H_2$ complex stands out as a significant nonradiative recombination center in $FASnI_3$-based perovskite solar cells.

The above-analyzed findings offer valuable information for improving the performance of $FASnI_3$-based solar cells and other related optoelectronic devices. That is, it would be significant to mitigate the nonradiative recombination rate by reducing the density of $V_{Sn}-H_2$. The formation of such a defect is sensitive to the quantity of Sn and H during the growth and post-processing. This explains the experimental observation of different nonradiative recombination rates (the range of $10^7 \sim 10^9\ s^{-1}$) for the $FASnI_3$ active layers even that were synthesized with the same SnI_2/FAI ratio in the precursors [15,20,21,44]. Therefore, to effectively suppress the nonradiative recombination induced by $V_{Sn}-H_2$, in addition to the commonly used Sn-rich strategy, minimizing unintentional H contamination would be also a critical step, such as building an effective H-blocking layer between the organic transporting materials and the perovskite active layers as well as avoiding the H-rich solvents and additives.

Conclusion

In summary, our first-principles calculations unveil a significant nonradiative recombination center in $FASnI_3$ and the related solar cells. The general and abundant native Sn vacancies can effectively trap hydrogen and form $V_{Sn}-H_2$ complexes. The resultant $V_{Sn}-H_2$ complexes behave as effective nonradiative recombination centers in $FASnI_3$ and induce significant energy loss. Therefore, the combined Sn-rich and H-poor growth conditions are proposed to be critical for further enhancing the related-device performance. This work identifies an important microscopic origin of the nonradiative recombination losses in the Sn-based halide perovskite materials and provides valuable information for future developments of the nontoxic Sn-based perovskite solar cells and other broad device applications.

Computational method

First-principles calculations are performed based on density functional theory (DFT) as implemented in the Vienna Ab initio Simulation Package (VASP) [54]. Projector augmented wave (PAW) pseudopotentials [55] were employed. We studied $FASnI_3$ in a cubic (Pm3m) crystal structure [56]. A plane-wave energy cutoff of 400 eV and a Monkhors–Pack sampling of 2 × 2 × 2 k-points were used for the 3 × 2 × 2 supercells with 144 atoms. Tkatchenko-Scheffler (TS) scheme [57] was used to describe the dispersion interactions for the hybrid perovskite system [58]. All atoms are relaxed until the forces on atoms are below 0.01 eV/Å. Heyd–Scuseria–Ernzerhof hybrid functional ($\alpha = 0.43$) including the spin-orbit coupling (HSE+SOC) was used for the defect calculations, which can reproduce the bandgap value of 1.38 eV (see **Figure S4** for the band structures of $FASnI_3$ with HSE and HSE+SOC), compared with the experimental results of 1.40 eV [13].

For a defect ionized the charge state q, its formation energy, $\Delta H_f\left(\mathrm{D}_\mathrm{i}^\mathrm{q}\right)$, is calculated by [50]:

$$\Delta H_f\left(\mathrm{D}_\mathrm{i}^\mathrm{q}\right) = E\left(\mathrm{D}_\mathrm{i}^\mathrm{q}\right) - E(host) - \Sigma n_i(\mu_i + \Delta\mu_i) + q\left(E_f + E(VBM) + \Delta V\right) + \Delta_{corr}^{q}$$

(1)

Here, $E\left(\mathrm{D}_\mathrm{i}^\mathrm{q}\right)$ and $E(host)$ are the total energies of the defect-containing and defect-free supercells, respectively; n_i and q are the differences in the number of atoms and charge states between the defect-containing and defect-free supercells, respectively. μ_i stands for the absolute value of the chemical potential of defect atoms. $\Delta\mu_i$ stands for the relative value of the chemical potential, which is related to growth conditions. Specifically, bounds can be placed on the range of relative chemical potentials by choosing values that ensure thermodynamic stability of $FASnI_3$ and prevent the formation of secondary common competing phases (FAI, SnI_2, SnI_4, and FA_2SnI_6):

$$\Delta\mu_{FA} + \Delta\mu_{Sn} + 3\Delta\mu_I = \Delta H_f(FASnI_3)$$

$$\Delta\mu_{FA} + \Delta\mu_I \leq \Delta H_f(FAI)$$

$$\Delta\mu_{Sn} + 2\Delta\mu_I \leq \Delta H_f(SnI_2)$$

$$\Delta\mu_{Sn} + 4\Delta\mu_I \leq \Delta H_f(SnI_4)$$

$$2\Delta\mu_{FA} + \Delta\mu_{Sn} + 6\Delta\mu_I \leq \Delta H_f(FA_2SnI_6)$$

E_f is the Fermi energy referenced to the valence band maximum (VBM), and $E(VBM)$ represents the energy of the VBM of the host material. ΔV is used for ensuring the alignment of the potential for the charged defect in supercells and Δ^q_{corr} stands for the finite-size correction term for the periodic images of the charged defects [59]. The transition energy level is defined as the Fermi-level position for which the formation energies of different defect states are equal and can be given by:

$$\mathcal{E}(q/q') = \left[\Delta H_f\left(\mathrm{D_i^q}, E_f = 0\right) - \Delta H_f\left(\mathrm{D_i^{q'}}, E_f = 0\right)\right] / (q' - q) \tag{2}$$

The defect concentration at thermal equilibrium can be given by [50]: $N = N_0 e^{-\frac{\Delta H}{kT}}$, where N_0 stands for the number of available sites for defect formation in the CsPbI$_3$ lattice per volume, ΔH is the formation energy of defect, k is the Boltzmann constant, and T is temperature.

The calculation of nonradiative capture coefficients is performed using the NONRAD package [43,47], which is based on the well-established multi-phonon emission methodology, and includes the effects of anharmonicity by directly solving the one-dimensional Schrödinger equation using the Fourier grid method [39,60]. The potential energy surfaces are obtained by interpolating the energies from first-principles calculations. The electron-phonon coupling matrix elements for electron and hole capture are evaluated within the linear-coupling approximation using the PAW as implemented in the VASP.

Acknowledgments

We acknowledge the expert support provided by the Sydney Informatics Hub (SIH) team—a core research facility of the University of Sydney. This work was supported by computational resources provided by the Australian Government through Gadi under the National Computational Merit Allocation Scheme and was accessed through the SIH HPC Allocation Scheme [LE190100021]. We acknowledge partial financial supports from the Australian Research Council [DP200100940] and [DE180100167].

Declaration of interests

The authors declare no competing interests.

Data availability

The data that support the findings of this study are available from the corresponding author upon reasonable request.

Author information

Contributions: *Yuhang Liang*, *Xiangyuan Cui*, and *Rongkun Zheng* conceived the idea. *Yuhang Liang* performed the DFT computations under the supervision of *Xiangyuan Cui* and *Rongkun Zheng*. All authors contributed to the discussion and writing of the paper.

Corresponding authors: Correspondence to *Xiangyuan Cui* (carl.cui@sydney.edu.au), *Jun Huang* (jun.huang@sydney.edu.au), or *Rongkun Zheng* (rongkun.zheng@sydney.edu.au)

Reference

[1] Y. Cao et al., *Perovskite Light-Emitting Diodes Based on Spontaneously Formed Submicrometre-Scale Structures*, Nature **562**, 7726 (2018).

[2] Y. C. Kim, K. H. Kim, D.-Y. Son, D.-N. Jeong, J.-Y. Seo, Y. S. Choi, I. T. Han, S. Y. Lee, and N.-G. Park, *Printable Organometallic Perovskite Enables Large-Area, Low-Dose X-Ray Imaging*, Nature **550**, 87 (2017).

[3] J. Jeong et al., *Pseudo-Halide Anion Engineering for α-FAPbI 3 Perovskite Solar Cells*, Nature **592**, 7854 (2021).

[4] H. Min et al., *Perovskite Solar Cells with Atomically Coherent Interlayers on SnO2 Electrodes*, Nature **598**, 444 (2021).

[5] L. Meng, J. You, and Y. Yang, *Addressing the Stability Issue of Perovskite Solar Cells for Commercial Applications*, Nat. Commun. **9**, 5265 (2018).

[6] W. Ke, C. C. Stoumpos, and M. G. Kanatzidis, *"Unleaded" Perovskites: Status Quo and Future Prospects of Tin-Based Perovskite Solar Cells*, Adv. Mater. **31**, 1803230 (2019).

[7] Y. Liang, F. Li, and R. Zheng, *Low-Dimensional Hybrid Perovskites for Field-Effect Transistors with Improved Stability: Progress and Challenges*, Adv. Electron. Mater. **6**, 2000137 (2020).

[8] J. Cao and F. Yan, *Recent Progress in Tin-Based Perovskite Solar Cells*, Energy Environ. Sci. **14**, 1286 (2021).

[9] W. Shockley and H. J. Queisser, *Detailed Balance Limit of Efficiency of P-n Junction Solar Cells*, J. Appl. Phys. **32**, 510 (1961).

[10] I. Chung, B. Lee, J. He, R. P. H. Chang, and M. G. Kanatzidis, *All-Solid-State Dye-Sensitized Solar Cells with High Efficiency*, Nature **485**, 486 (2012).

[11] S. Shao, J. Liu, G. Portale, H.-H. Fang, G. R. Blake, G. H. ten Brink, L. J. A. Koster, and M. A. Loi, *Highly Reproducible Sn-Based Hybrid Perovskite Solar Cells with 9% Efficiency*, Adv. Energy Mater. **8**, 1702019 (2018).

[12] N. K. Noel et al., *Lead-Free Organic–Inorganic Tin Halide Perovskites for Photovoltaic Applications*, Energy Environ. Sci. **7**, 3061 (2014).

[13] Z. Zhu, X. Jiang, D. Yu, N. Yu, Z. Ning, and Q. Mi, *Smooth and Compact FASnI3 Films for Lead-Free Perovskite Solar Cells with over 14% Efficiency*, ACS Energy Lett. **7**, 2079 (2022).

[14] L. Ma, F. Hao, C. C. Stoumpos, B. T. Phelan, M. R. Wasielewski, and M. G. Kanatzidis, *Carrier Diffusion Lengths of over 500 Nm in Lead-Free Perovskite CH3NH3SnI3 Films*, J. Am. Chem. Soc. **138**, 14750 (2016).

[15] X. Meng, Y. Li, Y. Qu, H. Chen, N. Jiang, M. Li, D.-J. Xue, J.-S. Hu, H. Huang, and S. Yang, *Crystallization Kinetics Modulation of FASnI3 Films with Pre-Nucleation Clusters for Efficient Lead-Free Perovskite Solar Cells*, Angew. Chem. Int. Ed. **60**, 3693 (2021).

[16] L. He, H. Gu, X. Liu, P. Li, Y. Dang, C. Liang, L. K. Ono, Y. Qi, and X. Tao, *Efficient Anti-Solvent-Free Spin-Coated and Printed Sn-Perovskite Solar Cells with Crystal-Based Precursor Solutions*, Matter **2**, 167 (2020).

[17] C. H. Ng, K. Hamada, G. Kapil, M. A. Kamarudin, Z. Wang, S. Likubo, Q. Shen, K. Yoshino, T. Minemoto, and S. Hayase, *Reducing Trap Density and Carrier Concentration by a Ge Additive for an Efficient Quasi 2D/3D Perovskite Solar Cell*, J. Mater. Chem. A **8**, 2962 (2020).

[18] C. H. Ng et al., *Role of GeI2 and SnF2 Additives for SnGe Perovskite Solar Cells*, Nano Energy **58**, 130 (2019).

[19] D. Meggiolaro, S. G. Motti, E. Mosconi, A. J. Barker, J. Ball, C. A. R. Perini, F. Deschler, A. Petrozza, and F. D. Angelis, *Iodine Chemistry Determines the Defect Tolerance of Lead-Halide Perovskites*, Energy Environ. Sci. **11**, 702 (2018).

[20] R. L. Milot, M. T. Klug, C. L. Davies, Z. Wang, H. Kraus, H. J. Snaith, M. B. Johnston, and L. M. Herz, *The Effects of Doping Density and Temperature on the Optoelectronic Properties of Formamidinium Tin Triiodide Thin Films*, Adv. Mater. **30**, 1804506 (2018).

[21] M. B. Johnston and L. M. Herz, *Hybrid Perovskites for Photovoltaics: Charge-Carrier Recombination, Diffusion, and Radiative Efficiencies*, Acc. Chem. Res. **49**, 146 (2016).

[22] Q. Tai, J. Cao, T. Wang, and F. Yan, *Recent Advances toward Efficient and Stable Tin-Based Perovskite Solar Cells*, EcoMat **1**, e12004 (2019).

[23] W.-F. Yang, F. Igbari, Y.-H. Lou, Z.-K. Wang, and L.-S. Liao, *Tin Halide Perovskites: Progress and Challenges*, Advanced Energy Materials **10**, 1902584 (2020).

[24] Q. Zhang et al., *Stable Lead-Free Tin Halide Perovskite with Operational Stability >1200 h by Suppressing Tin(II) Oxidation*, Angewandte Chemie International Edition **n/a**, e202205463 (n.d.).

[25] M. H. Kumar et al., *Lead-Free Halide Perovskite Solar Cells with High Photocurrents Realized Through Vacancy Modulation*, Adv. Mater. **26**, 7122

(2014).

[26] T. Shi, H.-S. Zhang, W. Meng, Q. Teng, M. Liu, X. Yang, Y. Yan, H.-L. Yip, and Y.-J. Zhao, *Effects of Organic Cations on the Defect Physics of Tin Halide Perovskites*, J. Mater. Chem. A **5**, 15124 (2017).

[27] C. G. Van de Walle and J. Neugebauer, *Universal Alignment of Hydrogen Levels in Semiconductors, Insulators and Solutions*, Nature **423**, 6940 (2003).

[28] C. G. Van de Walle and J. Neugebauer, *Hydrogen in Semiconductors*, Annu. Rev. Mater. Res. **36**, 179 (2006).

[29] D. R. Ceratti, A. Zohar, R. Kozlov, H. Dong, G. Uraltsev, O. Girshevitz, I. Pinkas, L. Avram, G. Hodes, and D. Cahen, *Eppur Si Muove: Proton Diffusion in Halide Perovskite Single Crystals*, Adv. Mater. **32**, 2002467 (2020).

[30] S. Sadhu, T. Buffeteau, S. Sandrez, L. Hirsch, and D. M. Bassani, *Observing the Migration of Hydrogen Species in Hybrid Perovskite Materials through D/H Isotope Exchange*, J. Am. Chem. Soc. **142**, 10431 (2020).

[31] C. Cardenas-Daw, T. Simon, J. K. Stolarczyk, and J. Feldmann, *Migration of Constituent Protons in Hybrid Organic–Inorganic Perovskite Triggers Intrinsic Doping*, J. Am. Chem. Soc. **139**, 16462 (2017).

[32] D. A. Egger, L. Kronik, and A. M. Rappe, *Theory of Hydrogen Migration in Organic-Inorganic Halide Perovskites*, Angew. Chem. Int. Ed. **54**, 12437 (2015).

[33] Y. Liang, X. Cui, F. Li, C. Stampfl, S. P. Ringer, and R. Zheng, *Atomic and Molecular Hydrogen Impurities in Hybrid Perovskite Solar Cells*, J. Phys. Chem. C **126**, 1721 (2022).

[34] Y. Liang, X. Cui, F. Li, C. Stampfl, J. Huang, S. P. Ringer, and R. Zheng, *Hydrogen-Anion-Induced Carrier Recombination in MAPbI3 Perovskite Solar Cells*, J. Phys. Chem. Lett. **12**, 10677 (2021).

[35] Y. Liang, X. Cui, F. Li, C. Stampfl, S. P. Ringer, J. Huang, and R. Zheng, *Minimizing and Controlling Hydrogen for Highly Efficient Formamidinium Lead Triiodide Solar Cells*, J. Am. Chem. Soc. **144**, 6770 (2022).

[36] Y. Liang, X. Cui, F. Li, C. Stampfl, S. P. Ringer, J. Huang, and R. Zheng, *Hydrogen-Induced Nonradiative Recombination in All-Inorganic CsPbI3 Perovskite Solar Cells*, Solar RRL **n/a**, 2200211 (n.d.).

[37] Y. Liang, X. Cui, F. Li, C. Stampfl, S. P. Ringer, J. Huang, and R. Zheng, *Interstitial Hydrogen Anions: A Cause of p-Type Conductivity in CsSnI3*, J. Phys. Chem. C (2022).

[38] B. Park and S. I. Seok, *Intrinsic Instability of Inorganic–Organic Hybrid Halide Perovskite Materials*, Adv. Mater. **31**, 1805337 (2019).

[39] X. Zhang, M. E. Turiansky, J.-X. Shen, and C. G. Van de Walle, *Iodine Interstitials as a Cause of Nonradiative Recombination in Hybrid Perovskites*, Phys. Rev. B **101**, 140101 (2020).

[40] D. Meggiolaro, D. Ricciarelli, A. A. Alasmari, F. A. S. Alasmary, and F. De Angelis, *Tin versus Lead Redox Chemistry Modulates Charge Trapping and Self-Doping in Tin/Lead Iodide Perovskites*, J. Phys. Chem. Lett. **11**, 3546 (2020).

[41] S. Tao, I. Schmidt, G. Brocks, J. Jiang, I. Tranca, K. Meerholz, and S. Olthof, *Absolute Energy Level Positions in Tin- and Lead-Based Halide Perovskites*, Nat Commun **10**, 1 (2019).

[42] E. V. Lavrov, F. Herklotz, and J. Weber, *Identification of Two Hydrogen Donors in ZnO*, Phys. Rev. B **79**, 165210 (2009).

[43] A. Alkauskas, Q. Yan, and C. G. Van de Walle, *First-Principles Theory of Nonradiative Carrier Capture via Multiphonon Emission*, Phys. Rev. B **90**, 075202 (2014).

[44] X. Meng, T. Wu, X. Liu, X. He, T. Noda, Y. Wang, H. Segawa, and L. Han, *Highly Reproducible and Efficient FASnI3 Perovskite Solar Cells Fabricated with Volatilizable Reducing Solvent*, J. Phys. Chem. Lett. **11**, 2965 (2020).

[45] X. Meng, J. Lin, X. Liu, X. He, Y. Wang, T. Noda, T. Wu, X. Yang, and L. Han, *Highly Stable and Efficient FASnI3-Based Perovskite Solar Cells by Introducing Hydrogen Bonding*, Advanced Materials **31**, 1903721 (2019).

[46] B. Subedi, C. Li, M. M. Junda, Z. Song, Y. Yan, and N. J. Podraza, *Effects of Intrinsic and Atmospherically Induced Defects in Narrow Bandgap (FASnI3)x(MAPbI3)1−x Perovskite Films and Solar Cells*, J. Chem. Phys. **152**, 064705 (2020).

[47] M. E. Turiansky, A. Alkauskas, M. Engel, G. Kresse, D. Wickramaratne, J.-X. Shen, C. E. Dreyer, and C. G. Van de Walle, *Nonrad: Computing Nonradiative Capture Coefficients from First Principles*, Comput. Phys. Commun. **267**, 108056 (2021).

[48] G. Nasti and A. Abate, *Tin Halide Perovskite (ASnX3) Solar Cells: A Comprehensive Guide toward the Highest Power Conversion Efficiency*, Advanced Energy Materials **10**, 1902467 (2020).

[49] X. Zhang, J.-X. Shen, and C. G. Van de Walle, *First-Principles Simulation of Carrier Recombination Mechanisms in Halide Perovskites*, Advanced Energy Materials **10**, 1902830 (2020).

[50] J. Kang, J. Li, and S.-H. Wei, *Atomic-Scale Understanding on the Physics and Control of Intrinsic Point Defects in Lead Halide Perovskites*, Applied Physics Reviews **8**, 031302 (2021).

[51] Y. Chen and H. Zhou, *Defects Chemistry in High-Efficiency and Stable Perovskite Solar Cells*, Journal of Applied Physics **128**, 060903 (2020).

[52] Y. Shao, Y. Yuan, and J. Huang, *Correlation of Energy Disorder and Open-Circuit Voltage in Hybrid Perovskite Solar Cells*, Nat Energy **1**, 1 (2016).

[53] D. Ricciarelli, D. Meggiolaro, F. Ambrosio, and F. De Angelis, *Instability of Tin Iodide Perovskites: Bulk p-Doping versus Surface Tin Oxidation*, ACS Energy Lett. **5**, 2787 (2020).

[54] G. Kresse and J. Furthmüller, *Efficiency of Ab-Initio Total Energy Calculations for Metals and Semiconductors Using a Plane-Wave Basis Set*, Comput. Mater. Sci. **6**, 15 (1996).

[55] G. Kresse and D. Joubert, *From Ultrasoft Pseudopotentials to the Projector Augmented-Wave Method*, Phys. Rev. B **59**, 1758 (1999).

[56] S. Kahmann, O. Nazarenko, S. Shao, O. Hordiichuk, M. Kepenekian, J. Even, M. V. Kovalenko, G. R. Blake, and M. A. Loi, *Negative Thermal Quenching in FASnI3 Perovskite Single Crystals and Thin Films*, ACS Energy Lett. **5**, 2512 (2020).

[57] A. Tkatchenko and M. Scheffler, *Accurate Molecular Van Der Waals Interactions from Ground-State Electron Density and Free-Atom Reference Data*, Phys. Rev. Lett. **102**, 073005 (2009).

[58] C. Motta, F. El-Mellouhi, S. Kais, N. Tabet, F. Alharbi, and S. Sanvito, *Revealing the Role of Organic Cations in Hybrid Halide Perovskite CH3NH3PbI3*, Nat. Commun. **6**, 7026 (2015).

[59] C. Freysoldt, J. Neugebauer, and C. G. Van de Walle, *Fully Ab Initio Finite-Size Corrections for Charged-Defect Supercell Calculations*, Phys. Rev. Lett. **102**, 016402 (2009).

[60] X. Zhang, J.-X. Shen, M. E. Turiansky, and C. G. Van de Walle, *Minimizing Hydrogen Vacancies to Enable Highly Efficient Hybrid Perovskites*, Nat. Mater.

20, 971 (2021).